scientific reports

Check for updates

OPEN

Substrate-induced modulation of transient optical response of large-area monolayer MoS_2

Ashish Soni[1,2], Nagendra S. Kamath[1,2], Yun-Yang Shen[3], Harshita Seksaria[4], Abir De Sarkar[4], Wen-Hao Chang[3,5] & Suman Kalyan Pal[1,2]✉

The intrinsic properties of two-dimensional (2D) transition-metal dichalcogenides (TMDs) are profoundly influenced by their interface conditions. Engineering the TMD/substrate interface is crucial for harnessing the unique optoelectronic properties of 2D TMDs in device applications. This study delves into how the transient optical properties of monolayer (ML) MoS_2 are affected by the substrate and film preparation processes, specifically focusing on the generation and recombination pathways of photoexcited carriers. Our experimental and theoretical analyses reveal that induced strain and defects during transfer process play pivotal roles in shaping these optical properties. Through femtosecond transient absorption measurements, we uncover the impact of substrate alterations on the carrier trapping process in ML MoS_2. Moreover, we investigate exciton-exciton annihilation (EEA), demonstrating that the EEA rate varies with different substrates and significantly decreases at low temperatures (77 K). This research paves the way for customizing the optoelectronic properties of TMDs through strategic interface engineering, potentially leading to the creation of highly efficient electronic devices such as optoelectronic memory, light-emitting diodes, and photodetectors.

Keywords TMDs, Ultrafast transient absorption spectroscopy, Exciton-exciton annihilation, Carrier trapping, Substrate effect, Density functional theory

Two-dimensional (2D) semiconductors have garnered significant interest in the scientific community due to their unique electronic, optical, and physical properties. Among them, 2D TMDs are particularly promising candidates. They possess a direct bandgap in their MLs and exhibit strong light-matter interactions due to quantum confinement effects, resulting in high absorption and unusual spin-orbit coupling effects[1,2]. The binding energy of excitons in ML TMDs is considerably higher due to increased Coulomb interactions[3,4] and reduced dielectric screening[5]. Consequently, quasi-particles such as excitons[3,6], trion[7,8], and biexcitons[9] can exist in ML TMDs even at room temperature.

The high binding energy and enhanced stability of excitons make 2D TMDs excellent materials for lighting applications[10–12]. Additionally, TMDs are suitable for other atomically thin optoelectronic devices, including transistors[13], phototransistors[14], energy conversion[15,16], and storage devices[17]. Large-area ML TMDs are indispensable for realizing ultralight optoelectronic devices for practical and industrial applications[18–20]. However, the growth of large-area ML TMDs by chemical vapor deposition (CVD) requires high growth temperatures, suitable substrates, and precursors, which limits their potential applications[21,22]. To overcome these limitations, a viable method for device fabrication involving TMDs is the transfer of as-grown samples onto desired substrates. This layer transfer is also crucial for removing growth precursors to avoid unwanted doping[23], and fabrication of flexible[24] and heterostructure devices[25,26]. In principle, the scattering by impurities and defects at the TMD/substrate interface can affect carrier mobility, thereby altering the performance of TMD-based optoelectronic devices[27,28]. Previous reports suggest that transfer process can induce strain and charge doping, ultimately impacting the carrier mobility and electronic band structure of 2D TMDs[29,30]. The electronic structure of 2D TMDs changes due to induced strain during transfer process[31]. The bandgap of layered TMDs is reported to be reduced under non-uniform strain[32,33].

Understanding the dynamics of charge carriers in layered TMDs is fundamental for the realization of TMD-based electronic and optoelectronic devices. For light-emitting devices, non-radiative carrier recombination

[1]School of Physical Sciences, Indian Institute of Technology Mandi, Kamand, Mandi, Himachal Pradesh 175005, India. [2]Advanced Materials Research Centre, Indian Institute of Technology Mandi, Kamand, Mandi, Himachal Pradesh 175005, India. [3]Department of Electrophysics, National Yang Ming Chiao Tung University, Hsinchu 30010, Taiwan. [4]Institute of Nano Science and Technology, Knowledge City, Sector 81, Mohali 140306, India. [5]Research Center for Applied Sciences, Academia Sinica, Nankang, Taipei 11529, Taiwan. ✉email: suman@iitmandi.ac.in

channels, such as defect capturing and Auger recombination, are critical factors that diminish charge carrier lifetime and limit the emission quantum yield or brightness of optoelectronic devices[34–36]. In recent years, researchers have sought to increase the emission quantum yield of 2D TMDs using various electronic and chemical approaches[31,37,38]. These efforts have enhanced emission efficiency at lower excitation densities, but at higher densities, exciton-exciton annihilation (EEA) limits the emission yield. In this context, the effect of substrates on exciton dynamics in TMDs remains largely unexplored. Understanding how substrates influence EEA and subsequently impact excitonic lifetime is imperative for advancing high-performance optoelectronic devices based on 2D TMDs.

In this work, we employed femtosecond transient absorption (TA) spectroscopy to probe the substrate-induced effects on the dynamical behavior of excitons in ML MoS_2 supported on sapphire, quartz, and Si/SiO_2. Steady-state spectroscopic measurements reveal that the optical properties of as-grown MoS_2 are markedly different from transferred samples due to the creation of new defects during the transfer process. Density functional theory (DFT) was used to unveil the effect of induced strain on the optical properties of MoS_2. Our TA studies demonstrate that exciton dynamics in 2D MoS_2 depend not only on the substrate but also on the sample preparation process (as-grown or transferred). The EEA rate decreases significantly when MoS_2 grown on sapphire is transferred to a Si/SiO_2 substrate. Moreover, the EEA rate is temperature-dependent and reduces at low temperatures. We discuss plausible explanations for the variation of EEA rate with substrate and temperature, emphasizing the role of defect capturing and thermally assisted exciton-exciton interaction. This detailed study illuminates the complex interplay between substrate-induced defects and strain on exciton dynamics in 2D TMDs during transfer processes, offering critical insights for the advancement of optoelectronic devices.

Results and discussion

Optical and structural characterization

Large-area ML MoS_2 was grown on double-side polished (DSP) sapphire and subsequently transferred onto various substrates, including DSP quartz, DSP sapphire, and Si/SiO_2. Continuous ML MoS_2 films on these substrates are evident from the optical images depicted in Figure S1(a-d). The absorption (red curve) and photoluminescence (PL) (blue curve) spectra for all MoS_2 samples were measured at room temperature, as shown in Fig. 1a–d. Figure 1a indicates that the as-grown MoS_2 exhibits two distinct absorption peaks at 1.91 eV and 2.04 eV, corresponding to the A and B excitons, which arise from the optical transitions between the spin-split valence band (VB) and the conduction band (CB)[1,39,40]. The band nesting effect in ML MoS_2 leads to a C-exciton transition (according to Wilson and Yoffe's nomenclature), which becomes prominent at higher energies, around 2.87 eV[6,41].

The absorption spectra of the transferred samples are presented in Fig. 1b–d. In these samples, the A-exciton peak is observed to shift towards lower energy, with the shift following the order: DSP quartz (1.90 eV) to DSP sapphire (1.89 eV) to Si/SiO_2 (1.89 eV). The PL spectrum of as-grown ML MoS_2 shows emission peaks corresponding to the A (~ 1.86 eV) and B (~ 1.97 eV) excitons, as depicted in Fig. 1a. A broadening of the emission spectra (recorded under identical excitation energy) and the emergence of a shoulder peak (~ 1.75 eV) are observed in the transferred MoS_2 on sapphire and quartz substrates (Fig. 1b,c). This additional shoulder peak in the PL spectra of transferred MoS_2 could be attributed to either emission from defect states or trion emission, which will be discussed further. In contrast, the PL spectrum (recorded under identical excitation energy) of MoS_2 transferred onto Si/SiO_2 is similar to that of the as-grown sample.

The ML nature of our samples was confirmed using Raman spectroscopy and verified for homogeneity by optical microscopy (Figure S1). Thickness measurements, performed using atomic force microscopy (AFM), indicated that the thicknesses of the transferred samples are slightly greater than those of the as-grown MoS_2 (Figure S2). This increase in thickness is likely due to the formation of air bubbles between the layer and the substrate during the transfer process. The Raman spectrum of as-grown MoS_2 exhibits peaks at approximately 385.6 cm^{-1} and 405 cm^{-1}, corresponding to the in-plane (E^1_{2g}) and out-of-plane (A_{1g}) vibrations, respectively (Fig. 2a). The separation between these two peaks is about 19.4 cm^{-1}, confirming the monolayer nature of the MoS_2 film[42–45]. A small Raman peak observed at 419 cm^{-1} in both the as-grown and transferred samples on sapphire (Fig. 2a) is attributed to the Raman signature of the sapphire substrate[46,47]. In the transferred MoS_2 samples, the Raman peak corresponding to the E^1_{2g} mode shows a slight blueshift compared to the as-grown sample. This shift is attributed to strain release or defects in the transferred samples. The strain release in ML MoS_2 likely arises from variations in the thermal expansion coefficient during the transfer process[48–50]. It has been reported that strain primarily affects the in-plane vibration (E^1_{2g}) of MoS_2, while the out-of-plane vibration (A_{1g}) remains unaffected[51,52], which is consistent with our observations.

To investigate the impact of the change of substrate on PL properties of ML MoS_2, the emission spectra (recorded at room temperature under identical excitation energy) were fitted using a combination of Gaussian and Lorentzian (Voigt) functions. Theoretically, the linewidth broadening of excitonic PL in ML TMDs follows a Lorentzian shape. However, inhomogeneities introduced by ripples or bubbles require the inclusion of a Gaussian component to accurately model the spectra[53]. We found that a minimum of four components was necessary to adequately fit the PL spectra for all samples (Fig. 2b). The PL spectrum of as-grown MoS_2 displays distinct A and B-exciton peaks centered around ~ 1.86 eV and ~ 1.97 eV, respectively[1]. An additional peak at 1.81 eV is attributed to charged exciton or trion emission, as reported in previous studies[8,54]. Figure 2b shows that both A-exciton and trion emission peaks are red-shifted in the transferred MoS_2 samples. These red-shifts cannot be attributed to the release of strain when the MoS_2 layer was transferred to different substrates, as strain release typically results in a blue-shift in PL spectrum[55]. Instead, the observed red-shifts suggest the introduction of a different type of strain. While strain release generally causes a blue-shift in the PL spectrum, the prominent red-shift observed here indicates that other factors are at play. AFM mapping of the transferred samples (Figure

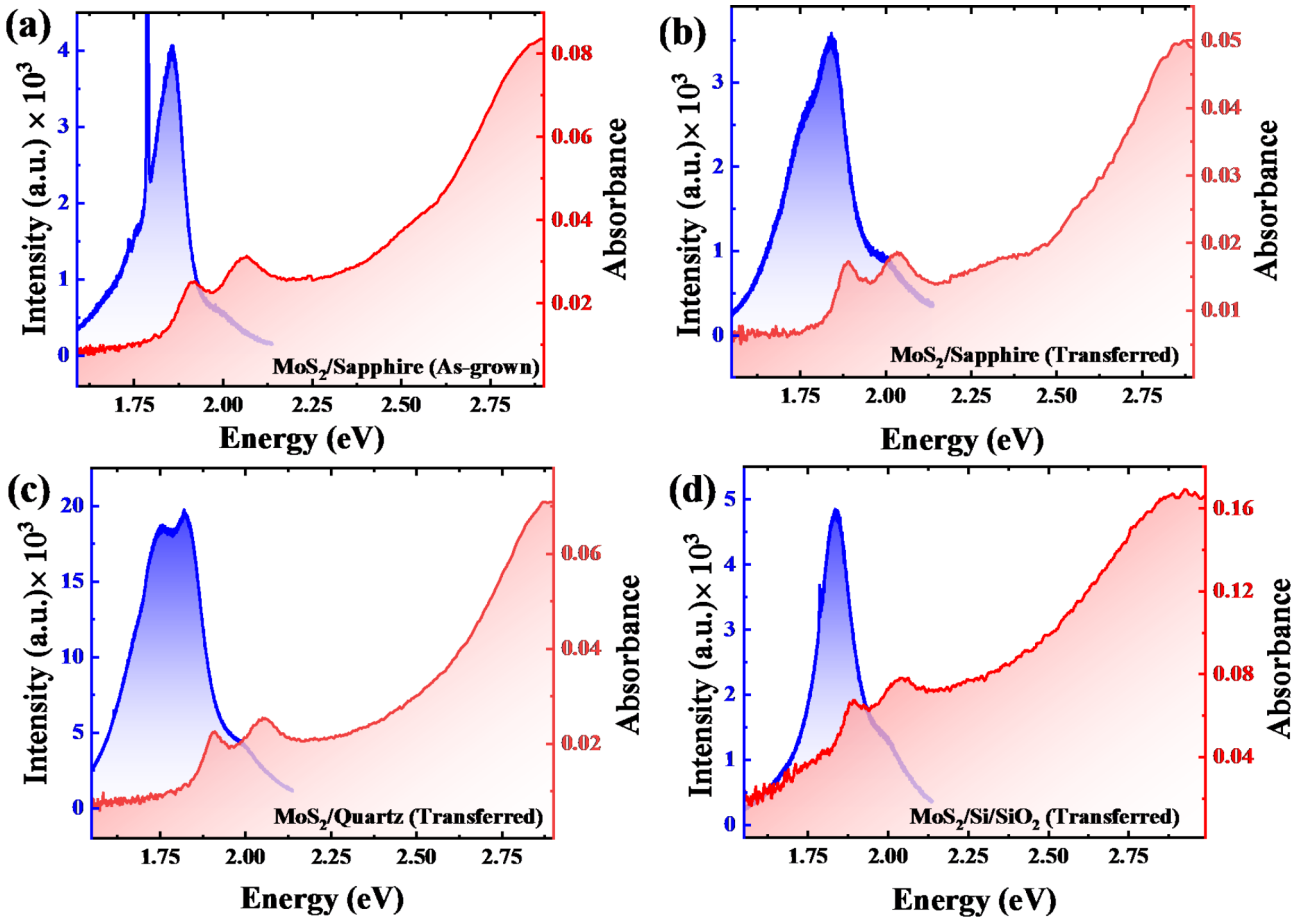

Fig. 1. Absorption (the red solid lines) and PL (the blue solid lines) spectra of CVD-grown large area ML MoS_2 (**a**) grown on sapphire and transferred on (**b**) sapphire, (**c**) quartz and (**d**) Si/SiO_2 substrates.

S3) reveals the presence of bubbles or ripples, which are likely responsible for the non-uniform strain. Therefore, the observed red-shift in the PL spectra is attributed to the non-uniform strain induced by these bubbles or ripples formed during the transfer process. Harats et al. reported a similar red-shift in the PL spectrum and trion formation due to non-uniform strain in WS_2, as predicted by the drift-diffusion model[56]. Various studies have investigated the impact of strain on the PL properties of ML MoS_2, indicating that the optical bandgap is modified by strain[33,57,58]. Additionally, the lowest energy peak in the PL spectra (labelled as "D") is attributed to emission from defect-bound excitons[59,60]. The relative contributions of A-exciton, B-exciton, trion, and defect emissions were determined from the fitting of PL spectra (Table S1). We found that the percentage of defect emission is higher in samples transferred onto sapphire (18%) and quartz (33%) substrates compared to Si/SiO_2 (13%) and the as-grown MoS_2 (12%). These results indicate a significant increase in defect states in MoS_2 transferred to sapphire and quartz substrates, in contrast to the sample transferred onto Si/SiO_2.

Theoretical modelling of strain induced by transfer processes

As previously discussed, the A-exciton absorption peak of ML MoS_2 shifts with transfer of the substrate. This shift is attributed to strain induced by the formation of ripples or bubbles and lattice parameters mismatch between the ML and the substrate[61,62]. To elucidate the effect of strain on the optical properties of MoS_2, we calculated the band structure of ML MoS_2 using density functional theory (DFT) under various tensile strains. Our calculations show that the bandgap of pristine MoS_2 decreases with increasing tensile strain (Figure S4), aligning with prior theoretical reports[45,63–65]. Additionally, to investigate the effects of specific substrates, we modelled MoS_2 placed on quartz and sapphire substrates (Fig. 3a,b). The lattice mismatches and associated strains are relatively small (1.2% for MoS_2/quartz and 3.5% for MoS_2/sapphire) while maintaining a hexagonal unit cell. The calculated bandgaps for MoS_2 on quartz and sapphire are 2.02 eV and 1.10 eV, respectively (Fig. 3c,d). The change in the calculated bandgap is significantly larger than the experimentally observed value. Several factors could contribute to this discrepancy. First, the experiments were conducted at room temperature (300 K), whereas the calculations were performed at 0 K. Second, only strain due to lattice mismatch was considered in the calculations, while other factors, such as ripples or bubbles present in actual samples, were not accounted for. However, DFT calculations exhibit the same trend of decreasing bandgap from quartz to sapphire as observed in the experiment (Fig. 1b,c), suggesting that strain can alter the bandgap of ML MoS_2.

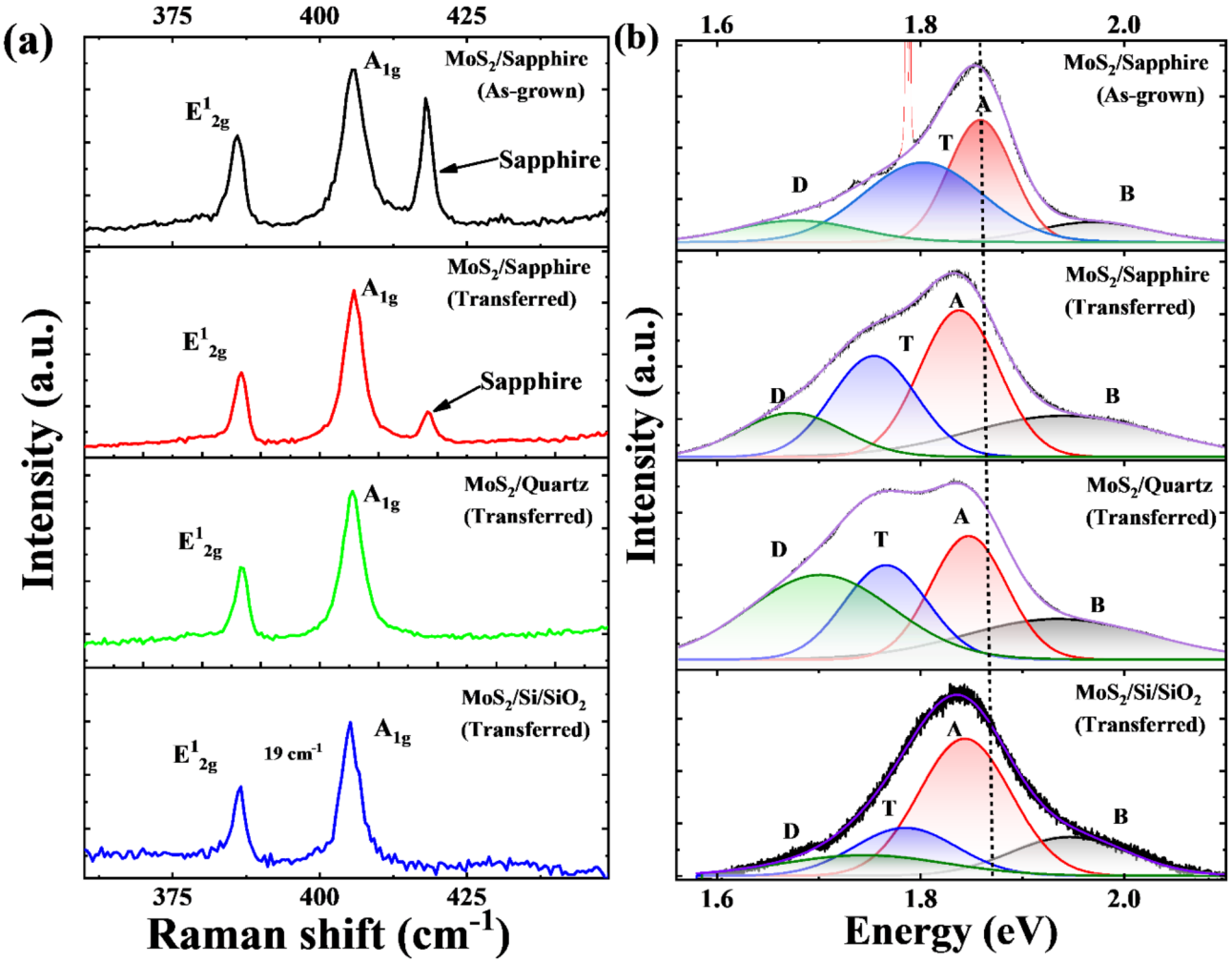

Fig. 2. (**a**) Raman spectra of ML MoS_2 on four different substrates. (**b**) Deconvolution of the PL spectra of as-grown and transferred ML MoS_2 into four curves (combination of Gaussian and Lorentzian). A, B, T, and D represent contributions of A-exciton, B-exciton, trion, and defect emission, respectively to the total PL.

X-ray photoelectron spectroscopy (XPS) study

The variation in the intensity of defect-related PL across different samples (Fig. 2b) suggests the presence of varying levels and types of defects in the ML MoS_2 samples. To quantitatively assess the presence of defects, we conducted X-ray photoelectron spectroscopy (XPS) measurements. High-resolution XPS spectra of Mo 3d for all samples are shown in Fig. 4a–d. The Mo 3d spectrum exhibits two prominent emission peaks at 232 eV (Mo $3d_{3/2}$) and 229.6 eV (Mo $3d_{5/2}$), corresponding to the Mo^{4+} state in MoS_2[66,67]. Moreover, a peak at 226.6 eV is attributed to the S 2s state, as reported previously[68,69]. Another small peak appears in all four samples around 236 eV with different intensities. This peak corresponds to the Mo^{6+} state, indicative of molybdenum oxides (MoO_3) formation[67]. The XPS spectra were fitted using a Voigt profile on a Shirley-type background to determine the contribution of each peak. The area under the oxide (Mo-O) peaks serves as a measure of oxidation-related defects in the samples. The percentage contributions (i.e., area integral percentages) of the Mo-O (Mo^{6+}) peaks, calculated from Fig. 4, are 13.9, 9.8, 10.2, and 20.2% for the as-grown and transferred MoS_2 on sapphire, quartz, and Si/SiO_2, respectively. These results indicate that the density of oxygen-related defects is comparatively lower in the transferred samples on sapphire and quartz compared to the as-grown and transferred samples on Si/SiO_2.

The as-grown MoS_2 samples on sapphire contain oxygen-related defects primarily due to the residual oxygen present during the CVD process or the deposition of unreacted MoO_3 on the sapphire surface[70,71]. However, during the transfer process, MoS_2 is moved from its original growth substrate to a new substrate (sapphire or quartz). The transfer process involves steps such as cleaning and annealing[72], which can reduce or eliminate these residuals and oxygen-related defects. As a result, the transferred MoS_2 samples on sapphire and quartz exhibit lower oxygen defect densities compared to the as-grown samples on sapphire.

Furthermore, we calculated the stoichiometric ratios of Mo to S from the XPS data (a detailed analysis is provided in the Supporting Information). We have found that the ratio of Mo: S is 1:1.9 in as-grown MoS_2 on sapphire, and 1:1.75, 1:1.7 and 1:1.88 in transferred MoS_2 on sapphire, quartz, and Si/SiO_2, respectively. Consequently, the estimated sulfur deficiency is 5%, 12.5%, 15%, and 6% for the as-grown MoS_2 on sapphire

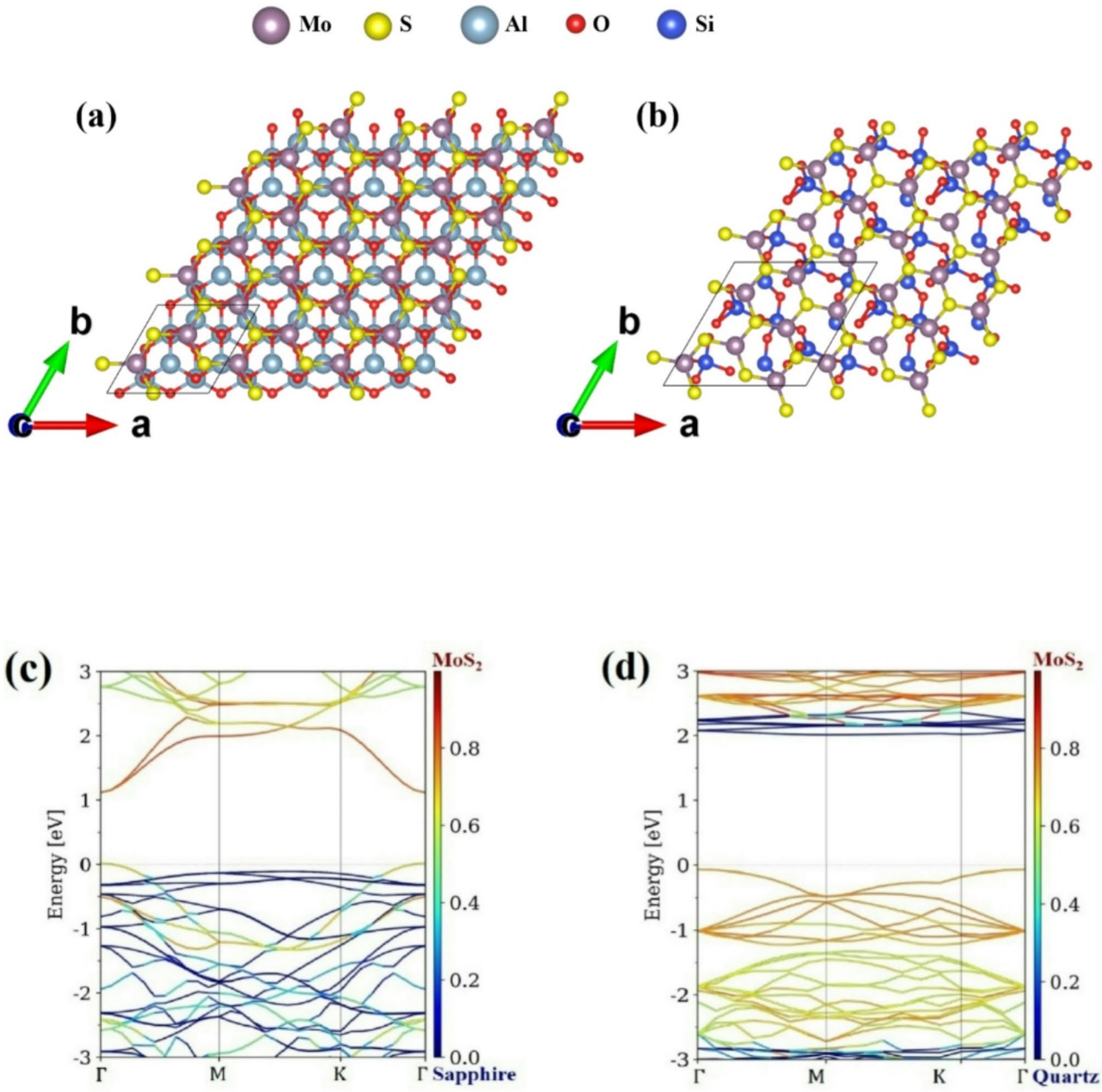

Fig. 3. The optimized structure of MoS_2 on top of (**a**) sapphire and (**b**) quartz. Band structure of (**c**) MoS_2/Sapphire and (**d**) MoS_2/Quartz calculated using DFT.

and for MoS_2 transferred onto sapphire, quartz, and Si/SiO_2, respectively. The XPS analysis indicates a notable increase in sulfur vacancies in the samples transferred onto sapphire and quartz. This observation correlates with the variation in defect-related PL intensity, where the defect-PL follows the trend: as-grown < Si/SiO_2 < sapphire < quartz. This trend is consistent with the increase in sulfur vacancies, suggesting that sulfur vacancies are the predominant defect type in transferred ML MoS_2 on sapphire and quartz.

Transient optical response

To investigate the influence of substrate material on exciton dynamics in ML MoS_2, we performed TA measurements on our samples. The TA spectra for as-grown ML MoS_2 on sapphire and transferred MoS_2 on various substrates, measured at both room temperature and at 77 K, are presented in Fig. 5a,b. The TA spectra exhibit two prominent features: ground state bleach (GSB) corresponding to A and B excitonic transitions and positive photoinduced absorption (PIA) observed on the low-energy side of the TA spectra (not present in MoS_2/Si/SiO_2). The appearance of GSB at exciton resonance is attributed to Pauli blocking[73,74]. Whereas, PIA is associated with phenomena such as carrier-induced broadening, biexciton formation, or free carrier absorption[75–77]. The

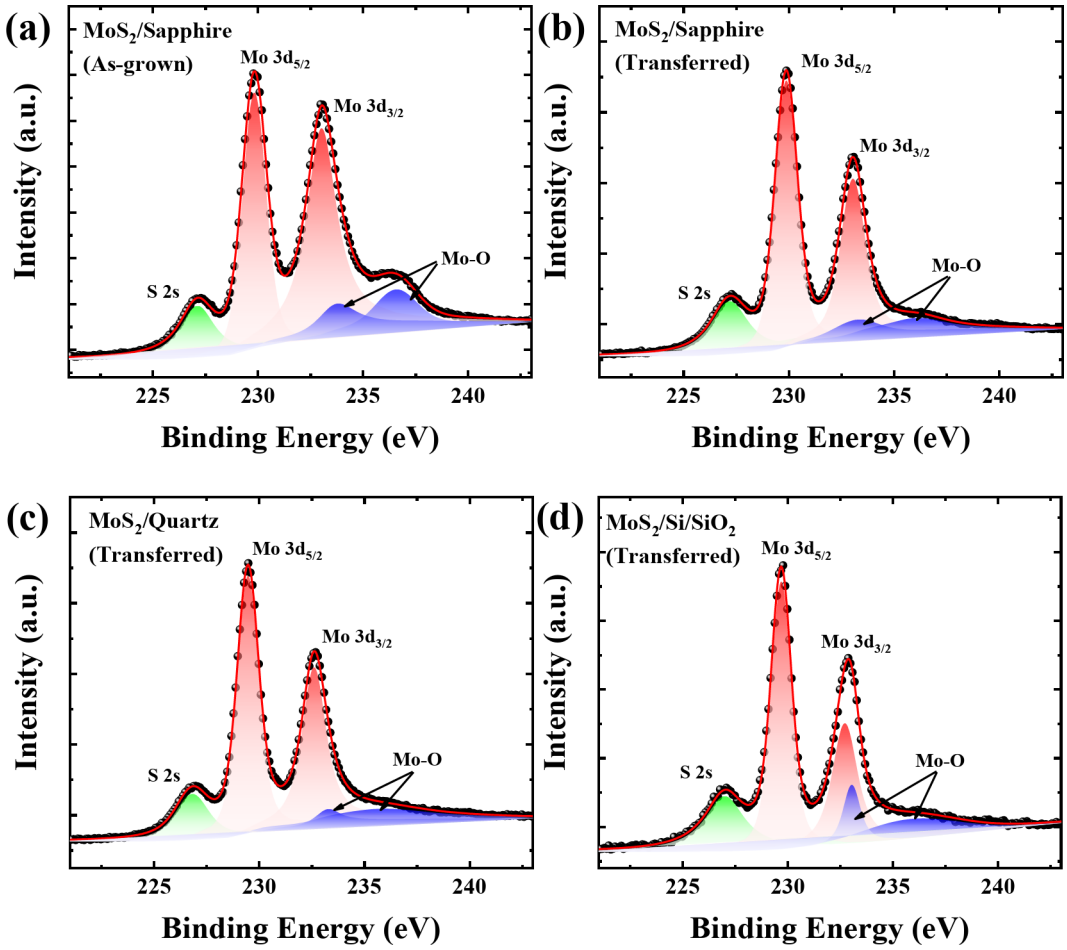

Fig. 4. XPS spectra of MoS_2 ML on (**a**) sapphire (as-grown), (**b**) sapphire (transferred), (**c**) quartz (transferred), (**d**) Si/SiO_2 (transferred) substrates with component peak-fitting. Red solid lines represent the overall fit to experimental data (black dots). The colour regions under the overall fitted curve show contributions of different states.

broadening of GSB bands in the TA spectra of transferred samples is notably more pronounced compared to that of the as-grown ML MoS_2 (Fig. 5a). This broadening can be attributed to an increased density of defect states in the transferred samples. We compared the decay kinetics of the A-exciton bleach across all samples (Fig. 5c) and observed that samples transferred onto sapphire and quartz display a positive ΔA signal following the initial negative bleach signal. Such a sign-changing behavior in the A-exciton bleach signal is commonly associated with mid-gap defect states in TMDs[78]. Therefore, the comparison of bleach kinetics suggests a higher density of mid-gap defect states in samples transferred onto sapphire and quartz compared to the other samples. These mid-gap defects are likely correlated with the higher density of sulfur vacancies, as indicated by the XPS analysis and supported by previous literature[79–81].

The bleach signals corresponding to the A and B excitonic transitions of as-grown MoS_2 exhibit a blue-shift at low temperature (Fig. 5b). This blue-shift is likely due to the suppression of electron-phonon interactions and lattice contraction, which results in an increased optical bandgap at lower temperatures[82–86]. Additionally, a shoulder feature around 1.86 eV appears in the A-exciton bleach of as-grown ML MoS_2 at low temperature (Fig. 5b). This shoulder could be attributed to charged excitons or defect-bound excitons[59,87]. However, trions (charged excitons) are typically formed after excitons, and thus, are unlikely to contribute to the bleach shoulder. Therefore, this shoulder peak is likely associated with excitons trapped by defect states within the ML MoS_2. In contrast, transferred samples on sapphire and quartz exhibit a splitting of the bleach band (Fig. 5b). The low-energy bleach component is attributed to excitons trapped in defect states, which have energy levels.

significantly below those of band-edge excitons. The observed splitting and appearance of separate bleach bands for trapped excitons at low temperature can be explained by the blue-shift of the A-exciton bleach due to the increase in bandgap and the reduced linewidth broadening of free and bound exciton transitions.

We compared the kinetics of the low-energy bleach band for all samples at low temperature (Fig. 5d). The negative ΔA followed by a high positive signal indicates a high density of defects in samples transferred onto sapphire and quartz. The TA kinetics at the split bands (1.83 and 1.89 eV) for MoS_2 on sapphire and quartz exhibit notable differences at 77 K (Figure S6). While ΔA remains negative for the high-energy bleach bands, it transitions to positive values for the low-energy bands. The prominent splitting of the A-exciton bleach band

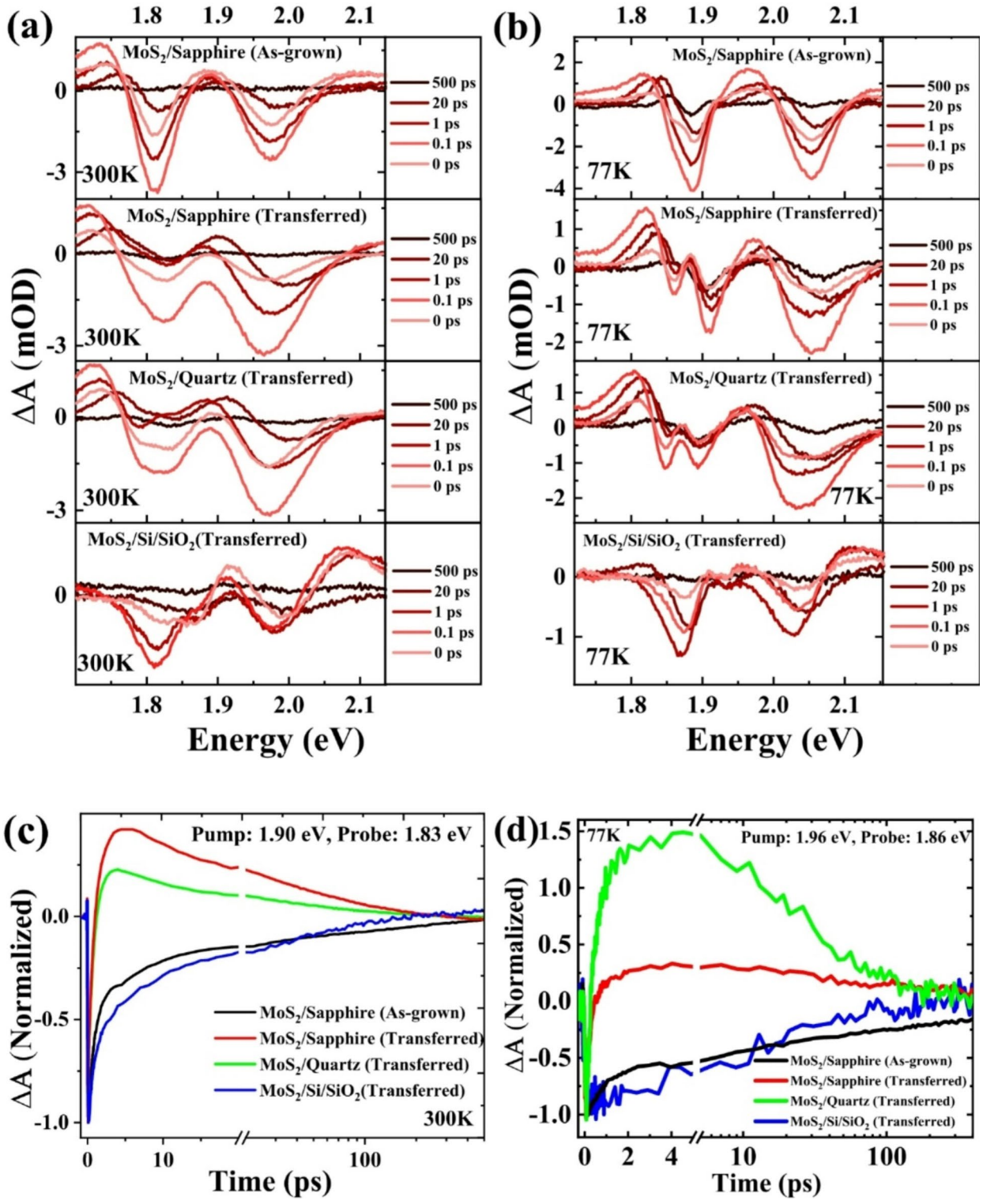

Fig. 5. TA spectra of as-grown and transferred ML MoS_2 (spot size of white light probe ~ $8.6 \times 10^{-4} cm^2$) at (**a**) room temperature (300 K) and (**b**) low temperature (77 K). The experiments were conducted at an excitation energy 2.33 eV and fluence 5.17×10^{-13}cm^{-2}. (**c**) Comparison of the decay kinetics of A-exciton at 300 K and (**d**) comparison of the decay kinetics of low energy bleach bands at 77 K. The spectra of the probe beams (generated from TOPAS) used for kinetics measurements are shown in Figure S6 (e, f).

at low temperature and the sign-changing behavior of ΔA suggest that the transient optical response of MoS_2 transferred onto sapphire and quartz is predominantly influenced by mid-gap defects, likely originating from sulfur vacancies.

Exciton capturing in ML MoS_2

Both steady-state and TA studies indicate that transferring ML MoS_2 onto different substrates introduces additional defects and strain into the MoS_2 layer. To further investigate the dynamical behavior of excitons under varying levels of strain and defect density, we performed TA kinetics measurements at different spectral positions. Figure 6a presents the excitation fluence-dependent decay kinetics of the A-exciton in as-grown MoS_2, using pump and probe photon energies of 1.9 and 1.83 eV, respectively, which are resonant with the A-excitonic transition. The TA kinetics were analyzed by fitting the data to the following exponential decay function (with $n = 3$),

$$\Delta A = \sum_{i=1}^{n} A_i exp(-t/T_i) \quad (1)$$

where, ΔA represents the differential absorption, As are preexponential factors, t stands for the time and T is the decay time of a particular exponential component.

The fitted curves are shown in Fig. 6a, and fitting parameters are provided in Table S2. We observed three decay components: a fast component (~ 0.26–0.34 ps), an intermediate component (~ 7–14 ps), and a slow component (~ 110–140 ps). The fast decay component, occurring on the sub-picosecond timescale, could be attributed to processes such as hot carrier cooling, carrier-phonon scattering, or carrier trapping by defect states[74,88]. Since the excitation energy was only slightly above the band edge, the generation of hot carriers is negligible.

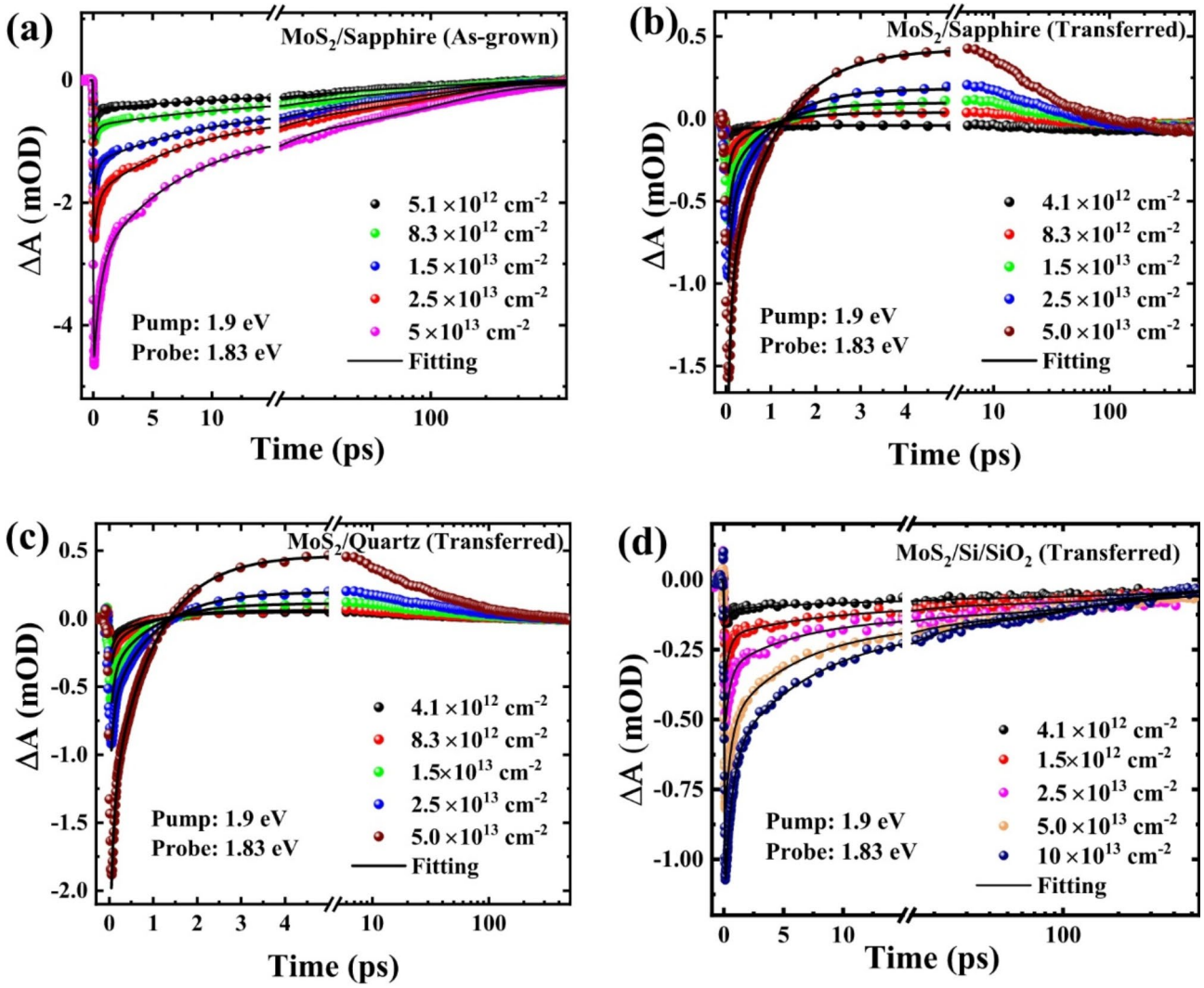

Fig. 6. Fluence-dependent TA kinetics measured at A-excitonic bleach of (**a**) as-grown and transferred ML MoS_2 on (**b**) sapphire, (**c**) quartz, and (**d**) Si/SiO_2 substrates at 300 K. The black lines are tri-exponential fits to experimental data.

Additionally, the time constant T_1 increases with excitation fluence and reaches a constant value, indicative of a defect-capturing process[89,90]. Therefore, T_1 is likely associated with the time required for excitons to be captured by defect states. The intermediate decay component (T_2) with a lifetime of ~ 7–13 ps, is characteristic of second-order relaxation processes such as Auger recombination, exciton-exciton annihilation (EEA)[89,91,92], and trion recombination[93]. The observed decrease in T_2 with increasing excitation fluence, accompanied by an increase in amplitude, suggests that this component is related to EEA. The slow component, with a time constant in the hundreds of picoseconds, is likely associated with radiative excitonic decay, as reported in the literature[44,92,94].

The decay kinetics of A-excitons in ML MoS_2 transferred onto sapphire and quartz exhibit distinct behaviors, as illustrated in Fig. 6b,c. In both cases, ΔA transitions from a negative to a positive value at high photon fluence. The initial part of the decay was fitted, revealing that a fast decay occurring on the sub-picosecond timescale (~ 0.07–0.1 ps) dominates the early decay (Table S3). According to previous studies, this behavior in TA kinetics could be attributed to PIA by trapped carriers in mid-gap defects, which can overshadow the bleach signal due to Pauli blocking[78,95]. Consequently, the positive shift in ΔA indicates a higher density of mid-gap defects in MoS_2 transferred onto sapphire and quartz compared to the as-grown sample. Conversely, the TA kinetics of MoS_2 transferred onto Si/SiO_2 (Fig. 6d) are similar to those of the as-grown MoS_2, showing no positive signal. This suggests that MoS_2 transferred onto Si/SiO_2, like the as-grown sample, has a lower density of sulfur defects. Recent studies suggest that the Si/SiO_2 substrate may passivate sulfur defects through adsorption O_2 at vacancy sites[79,96]. However, shallow traps due to oxygen vacancies still contribute to carrier decay in all samples. Therefore, the recombination dynamics of excitons and carriers in ML MoS_2 are influenced by both the substrate material and the preparation method (as-grown or transferred), due to the formation of varying concentrations of mid-gap and shallow defects. A schematic representation of the carrier dynamics, based on TA measurements, is illustrated in Fig. 7a alongside the band structure of ML MoS_2.

To quantify the capture time of carriers by defect states, we measured the kinetics of the PIA at 1.77 eV, which is attributed to absorption by trapped charges[89]. The fitting results for the growth kinetics at 1.77 eV are presented in Figure S7. The data indicate that the rise of the PIA signal at 1.77 eV is comparable to the initial sub-picosecond decay of the A-exciton bleach at the same fluence (Tables S2, S3, and S4). This observation further suggests that the PIA at 1.77 eV is associated with absorption by defect carriers. The rise time of the PIA signal reflects the carrier capture time by defect states. Comparison of the exciton capture times (Table 1) reveals that carrier capture is faster in MoS_2 transferred onto quartz and sapphire than in MoS_2 transferred onto Si/SiO_2 and as-grown samples. The higher density of mid-gap states in MoS_2 transferred onto quartz and sapphire likely accelerates the carrier capture rate in these samples.

Auger recombination of excitons

It is well known that in strongly confined systems such as quantum dots and 2D materials, strong optical excitation can result in the annihilation of excitons[97,98]. Due to enhanced Coulomb interactions, MoS_2 ML exhibits bound excitons, and strong exciton-exciton coupling results in EEA (at high excitation densities), which is a bimolecular process involving two or more excitons. Other second-order processes, such as biexciton formation, are negligible at the temperature investigated here (Fig. 6a,d)[99,100]. Additionally, the significant inhomogeneous broadening of the samples made it difficult to clearly differentiate between exciton and biexciton differential absorption. In the presence of EEA, the rate equation for a bimolecular recombination is described by[98,101]

$$\frac{dN\left(t\right)}{dt} = -\frac{1}{T}N\left(t\right) - \frac{1}{2}kN^2\left(t\right) \tag{2}$$

where N(t) denotes the exciton population at a time t, k represents the rate constant for EEA. The solution of this equation can, in principle, be utilized to analyze TA kinetics; however, for pedagogical clarity, we considered the two components separately. The first term of Eq. (2) represents first-order excitonic recombination, which dominates only at longer timescales. Conversely, EEA, being faster than monomolecular excitonic recombination, predominates at early times when the exciton density is high. Therefore, the annihilation rate can be determined by solving Eq. (2) considering only the second term. The solution to this rate equation is presented below.

$$N\left(t\right) = \frac{N_0}{1 + kN_0t}$$

$$\left(\frac{N_0}{N\left(t\right)} - 1\right) = \left(kN_0\right)t \tag{3}$$

where N_0 is the initial exciton density. We fitted the TA kinetics corresponding to A-excitons of ML MoS_2 grown on sapphire (Fig. 7b) and transferred on Si/SiO_2 (Fig. 7c) with Eq. (3). The values of EEA rates obtained from the fitting are presented in Table 2. A notable disparity in the EEA rates between the transferred ML MoS_2 and its as-grown counterpart was uncovered. Our findings suggest that the average EEA rate in transferred MoS_2 ($0.106 \pm 0.005\ cm^2/sec$) is lower than the as-grown ML ($0.204 \pm 0.002\ cm^2/sec$). This discrepancy further supports the notion that substrate-induced defects and strain significantly affect EEA. The introduction of defects during the transfer process serves as nonradiative recombination sites for excitons, competing with the annihilation process. Consequently, these defect states can alter the spatial distribution and mutual interaction of excitons, thereby influencing their probability of annihilation. The lower EEA rate in ML MoS_2 transferred on Si/SiO_2 could be a consequence of its higher density of oxygen defects (as evident from XPS measurements) compared to as-grown MoS_2. Moreover, induced strain during transfer process can modify the electronic band structure, affecting the exciton binding energy and subsequently influencing the formation, diffusion, and

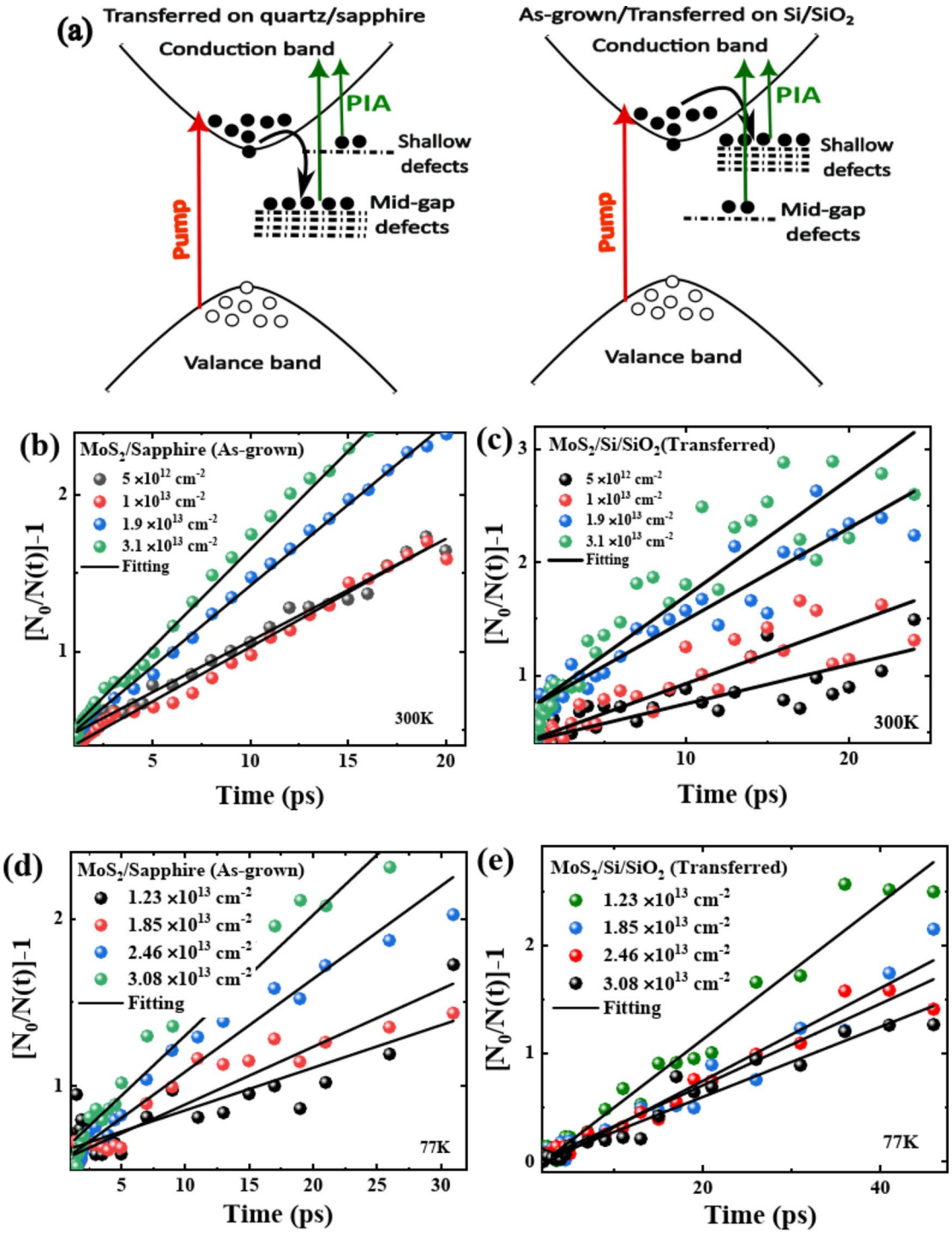

Fig. 7. (**a**) Schematic representation of the processes occurring in as-grown and transferred ML MoS_2 on Si/SiO_2 (right) and transferred on quartz and sapphire (left). Fitting of A-exciton kinetics of MoS_2 (**b**) as-grown on sapphire and (**c**) transferred on Si/SiO_2 substrates at room temperature with EEA model (Eq. 3). Fitting of A-exciton kinetics of MoS_2 (**d**) as-grown on sapphire and (**e**) transferred on Si/SiO_2 substrates at low temperature (77 K) with EEA model (Eq. 3).

Sample	MoS_2/Sapphire (As-grown)	MoS_2/Sapphire (Transferred)	MoS_2/Quartz (Transferred)	MoS_2/Si/SiO_2 (Transferred)
Defect-capturing time (ps)	0.32	0.07	0.08	0.41

Table 1. Defect-capturing time in ML MoS_2 on different substrates.

Fluence (cm^{-2})	EEA rate at 300 K (cm^2/sec)		Fluence (cm^{-2})	EEA rate at 77 K (cm^2/sec)	
	MoS_2/Sapphire (As-grown)	MoS_2/Si/SiO_2 (Transferred)		MoS_2/Sapphire (As-grown)	MoS_2/Si/SiO_2 (Transferred)
5.0×10^{12}	0.360 ± 0.002	0.145 ± 0.005	1.23×10^{13}	0.057 ± 0.003	0.024 ± 0.005
1.0×10^{13}	0.192 ± 0.002	0.118 ± 0.005	1.85×10^{13}	0.051 ± 0.003	0.029 ± 0.005
1.9×10^{13}	0.150 ± 0.002	0.092 ± 0.004	2.46×10^{13}	0.062 ± 0.003	0.019 ± 0.004
3.1×10^{13}	0.112 ± 0.002	0.067 ± 0.004	3.08×10^{13}	0.064 ± 0.003	0.013 ± 0.004
Average rate	0.204 ± 0.002	0.106 ± 0.005	Average rate	0.059 ± 0.003	0.021 ± 0.005

Table 2. EEA rates at different temperatures obtained by fitting GSB kinetics using EEA model (Eq. 3).

interaction of excitons. Thus, both strain and defects could play a pivotal role in determining the fluence range over which excitons do not undergo annihilation.

Furthermore, the A-exciton bleach kinetics of ML MoS_2 grown on sapphire (Fig. 7d) and transferred on Si/SiO_2 (Fig. 7e) measured at 77 K were fitted using Eq. (3). The average annihilation rates are found to be $0.059 \pm 0.003\ cm^2/sec$ for the MoS_2/Sapphire and $0.021 \pm 0.005\ cm^2/sec$ for the MoS_2/Si/SiO_2 (Table 2). Thus, the EEA rate is greatly reduced at low temperature. At low temperature, the thermal energy available to excitons decreases, leading to slower diffusion and a lower probability of exciton encounter, which in turn reduces the rate of annihilation. Additionally, the phonon population diminishes at low temperature, leading to a decrease in phonon-assisted exciton relaxation pathways. This reduction in phonon-mediated recombination processes could suppress EEA. It is noteworthy that the determination of the annihilation rate constant in the other two samples transferred on sapphire and quartz is not feasible because PIA signals due to trapped carriers supersede the bleach signal in the time window where EEA takes place (Fig. 6b,c).

It is evident from the above discussion that the interplay between defects and Auger-type recombination (EEA) plays a significant role in shaping the carrier dynamics in 2D materials like MoS_2. Recent studies have further highlighted the intricate relationships underlying these processes. For example, Wang et al.[102] highlighted the critical role of defect states in carrier trapping and their subsequent impact on recombination dynamics. Based on the dependence of the measured data on the pump fluence and temperature, they pointed out that other mechanisms of nonradiative recombination and carrier capture by defects are insignificant. Strong Coulomb interactions in 2D materials make Auger scattering more effective. Similarly, Shin et al.[103] provided in-depth analysis of how defect-induced trapping competes with Auger recombination, emphasizing the necessity of understanding these interactions for optimizing material performance.

Furthermore, the effects of strain on ultrafast exciton dynamics in 2D materials have garnered significant attention. Several recent studies[104–106] have shown that strain can dramatically influence exciton behavior, modifying lifetimes and recombination pathways. In this work, we observed that transfer-induced strain influences carrier dynamics in 2D MoS_2, contributing to the deeper understanding of strain engineering in 2D materials. Our findings demonstrate that transfer-induced strain can be a powerful tool to modulate exciton dynamics, with implications for the design of next-generation optoelectronic devices.

Our results highlight the critical role of sulfur vacancies in modulating the optical properties of MoS_2. The ability to control sulfur vacancies in MoS_2 by transferring it onto different substrates opens up promising avenues for future device applications[107]. These defects can enhance the electrical conductivity and carrier density of MoS_2, making it a promising material for use in electronic and optoelectronic devices[108]. For instance, sulfur vacancies have been shown to improve the performance of MoS_2-based transistors and sensors by increasing their sensitivity and response time[107,109]. Sulfur vacancies in MoS_2 introduce localized states within the bandgap, which can act as active sites for adsorption, enhancing the sensitivity and response time of sensors[110]. In the context of transistors, while defects are generally viewed as detrimental, controlled introduction of sulfur vacancies can lower the contact resistance and improve the charge carrier injection efficiency, this can lead to enhanced overall performance of the transistors[111]. Yin et al.[112] have shown that due to the strong trap effect, device based on TMDs can function as an infrared detector with high photoresponsivity and a high photo-switching ratio. It can also act as non-volatile optoelectronic memory with a high program/erase ratio and fast switching times. Additionally, the enhanced emission properties due to sulfur defects can be leveraged in developing more efficient LEDs and photodetectors[113]. Moreover, the ability to control sulfur vacancies offers pathways to tailor the electrical properties of MoS_2, making it an excellent candidate for next-generation transistors and flexible electronics[107,108]. The substrate-induced variations in sulfur vacancy densities can be strategically employed to design MoS_2-based devices with optimized performance and functionality[114,115]. The reduced EEA rate can improve the exciton lifetime, leading to higher device efficiency and stability[116,117]. By controlling the EEA rate through substrate choice and defect engineering, it is possible to tailor the optical and electronic properties of MoS_2, optimizing device performance for specific applications[118].

Conclusions

We have investigated the optical properties of ML MoS_2 grown on sapphire and transferred onto sapphire, quartz, and Si/SiO_2. Our comprehensive study, encompassing measurements of absorption, emission, and DFT calculations, reveals that substrate or air bubble-induced strains can modify the optical properties of MoS_2 by altering its band structure. XPS analysis unveils the presence of both sulfur and oxygen-induced defects in our samples, with defect PL increasing in MoS_2 transferred onto sapphire and quartz substrates due to an increased density of sulfur vacancies. Results from our femtosecond pump-probe spectroscopy measurements indicate

that both oxygen and sulfur vacancies govern the charge carrier dynamics. The carrier capture time depends on the substrate, primarily due to the variation in sulfur vacancies in as-grown and transferred MoS_2. Excitons decay via EEA at high excitation fluences, and at room temperature, the EEA rate of MoS_2 grown on sapphire (0.250 cm^2/sec) is much higher than that of MoS_2 transferred onto Si/SiO_2 (0.106 cm^2/sec). This change in the EEA rate could be attributed to substrate-induced defects (oxygen vacancies). Moreover, the EEA rate is greatly decreased at low temperature (77 K) due to a reduction in phonon-assisted exciton recombination. Leveraging the sensitivity of exciton dynamics in ML MoS_2 to the surrounding environment, particularly the substrate, offers promising avenues for further exploration and optimization of device design and performance.

Methodology

Sample preparation

ML MoS_2 films were grown on sapphire substrates by CVD in a horizontal 3-inch tube furnace. Molybdenum trioxide (MoO_3) and sulfur powders served as the growth reactants. The transition metal source and sapphire substrate were placed at the central high-temperature heating zone, while the sulfur powder was positioned upstream and heated with a heating belt. The ML MoS_2 was grown at 830 °C, with the sulfur temperature maintained at 132 °C. An argon (Ar) gas flow at 100 sccm was used as the carrier gas under a base pressure of 30 Torr during the growth process.

Transfer process

After CVD growth, the as-grown MoS_2 films were transferred from sapphire substrates to different target substrates (quartz, sapphire, and Si/SiO_2) using a wet transfer method with polymethyl methacrylate (PMMA) as a supporting layer. First, a layer of PMMA was spin-coated on the MoS_2 film grown on the sapphire substrate. The coated film was then soaked in a hot ammonia solution to detach the MoS_2 from the sapphire substrate. The detached MoS_2/PMMA was soaked in deionized water and subsequently picked up by the target substrate. After baking at 85 °C for 15 min, the sample was soaked in acetone and isopropyl alcohol to remove the PMMA layer.

Absorption, Raman and photoluminescence spectroscopy

The steady-state absorption spectrum was collected using a Shimadzu UV-2450 spectrometer (Agilent Technologies, USA). Photoluminescence (PL) and Raman measurements were performed at room temperature using Horiba Jobin-Yvon (Lab-RAM HR evolution) in the back-scattering configuration under an optical microscope. The samples were excited by a 532 nm laser through a 100X objective lens with a numerical aperture 0.9. The signals were analyzed by a monochromator and detected by an air-cooled CCD. The gratings with 300 and 1200 lines/mm were used for the PL and Raman measurements, respectively.

Femtosecond transient absorption (TA) spectroscopy

The TA spectroscopy system uses a femtosecond Ti: Sapphire amplifier (wavelength ~ 800 nm, repetition rate 1 kHz, and pulse width < 35 fs)[119]. The output from the amplifier (Spitfire Ace, Spectra physics) was divided into two components to generate pump and probe pulses. Pump pulses were obtained from the nonlinear optical parametric amplifier (TOPAS). The probe beam was a white light continuum (WLC) generated by focusing a small fraction of 800 nm light (from Spitfire Ace) on a CaF_2 crystal to obtain a stable and continuous white light probe. The probe beam was detected in both with and without pump conditions with the help of a mechanical chopper of frequency 500 Hz. A stepper motor was controlled the time delay between pump, and probe pulses with an optical delay line. TA spectra were recorded by dispersing the beam with a grating spectrograph (Acton Spectra Pro SP 2358) followed by a CCD array. Light pulses of particular wavelengths from another TOPAS were used as probes while measuring TA kinetics. Two photodiodes having variable gain were used to record TA kinetics. Low-temperature measurements were carried out using a temperature-controlled sample holder (Linkam Scientific Instruments, Model No. LTS420E-PB4) cooled with liquid nitrogen.

Data availability

The data that support the findings of this study are available from the corresponding author upon reasonable request.

Received: 22 October 2024; Accepted: 25 February 2025
Published online: 04 March 2025

References

1. Mak, K. F., Lee, C., Hone, J., Shan, J. & Heinz, T. F. Atomically thin MoS_2: A new direct-gap semiconductor. *Phys. Rev. Lett.* **105**, 136805 (2010).
2. Soni, A. & Pal, S. K. Valley degree of freedom in two-dimensional van der Waals materials. *J. Phys. D: Appl. Phys.* **55**, 303003 (2022).
3. Chernikov, A. et al. Exciton binding energy and nonhydrogenic rydberg series in monolayer WS_2. *Phys. Rev. Lett.* **113**, 076802 (2014).
4. Mayers, M. Z., Berkelbach, T. C., Hybertsen, M. S. & Reichman, D. R. Binding energies and spatial structures of small carrier complexes in monolayer transition-metal dichalcogenides via diffusion Monte Carlo. *Phys. Rev. B* **92**, 161404 (2015).
5. Lin, Y. et al. Dielectric screening of excitons and trions in single-layer MoS_2. *Nano Lett.* **14**, 5569–5576 (2014).
6. Vaquero, D. et al. Excitons, trions and Rydberg states in monolayer MoS_2 revealed by low-temperature photocurrent spectroscopy. *Commun. Phys.* **3**, 194 (2020).
7. Zhang, C., Wang, H., Chan, W., Manolatou, C. & Rana, F. Absorption of light by excitons and trions in monolayers of metal dichalcogenide MoS_2: Experiments and theory. *Phys. Rev. B* **89**, 205436 (2014).
8. Mak, K. F. et al. Tightly bound trions in monolayer MoS_2. *Nat. Mater.* **12**, 207–211 (2013).

9. You, Y. et al. Observation of biexcitons in monolayer WSe_2. *Nat. Phys.* **11**, 477–481 (2015).
10. Splendiani, A. et al. Emerging Photoluminescence in Monolayer MoS_2. *Nano Lett.* **10**, 1271–1275 (2010).
11. Mueller, T. & Malic, E. Exciton physics and device application of two-dimensional transition metal dichalcogenide semiconductors. *NPJ 2D Mater. Appl.* **2**, 29 (2018).
12. Zhao, H. et al. Strong optical response and light emission from a monolayer molecular crystal. *Nat. Commun.* **10**, 5589 (2019).
13. Baugher, B. W. H., Churchill, H. O. H., Yang, Y. & Jarillo-Herrero, P. Optoelectronic devices based on electrically tunable p–n diodes in a monolayer dichalcogenide. *Nat. Nanotechnol.* **9**, 262–267 (2014).
14. Amani, M. et al. Growth-substrate induced performance degradation in chemically synthesized monolayer MoS_2 field effect transistors. *Appl. Phys. Lett.* **104**, 203506 (2014).
15. Li, C. et al. Engineering graphene and TMDs based van der Waals heterostructures for photovoltaic and photoelectrochemical solar energy conversion. *Chem. Soc. Rev.* **47**, 4981–5037 (2018).
16. Yu, X. & Sivula, K. Toward large-area solar energy conversion with semiconducting 2D transition metal dichalcogenides. *ACS Energy Lett.* **1**, 315–322 (2016).
17. Wang, H., Feng, H. & Li, J. Graphene and graphene-like layered transition metal dichalcogenides in energy conversion and storage. *Small* **10**, 2165–2181 (2014).
18. Choi, W. et al. Recent development of two-dimensional transition metal dichalcogenides and their applications. *Mater. Today* **20**, 116–130 (2017).
19. Radisavljevic, B., Radenovic, A., Brivio, J., Giacometti, V. & Kis, A. Single-layer MoS_2 transistors. *Nat. Nanotechnol.* **6**, 147–150 (2011).
20. Luhar, B. et al. Charge transfer mediated photoluminescence engineering in WS_2 monolayers for optoelectronic application. *ACS Appl. Nano Mater.* **7**, 22350–22359 (2024).
21. Xie, Y. et al. Growth of monolayer WS_2 single crystals with atmospheric pressure CVD: Role of temperature. *MRS Adv.* **4**, 255–262 (2019).
22. Mandyam, S. V., Kim, H. M. & Drndić, M. Large area few-layer TMD film growths and their applications. *J. Phys.: Mater.* **3**, 024008 (2020).
23. Sharma, M., Singh, A., Aggarwal, P. & Singh, R. Large-area transfer of 2D TMDCs assisted by a water-soluble layer for potential device applications. *ACS Omega* **7**, 11731–11741 (2022).
24. Akinwande, D., Petrone, N. & Hone, J. Two-dimensional flexible nanoelectronics. *Nat. Commun.* **5**, 5678 (2014).
25. Cheng, J., Wang, C., Zou, X. & Liao, L. Recent advances in optoelectronic devices based on 2D materials and their heterostructures. *Adv. Opt. Mater.* **7**, 1800441 (2019).
26. Soni, A., Ghosal, S., Kundar, M., Pati, S. K. & Pal, S. K. Long-lived interlayer excitons in WS2/ruddlesden–popper perovskite van der waals heterostructures. *ACS Appl. Mater. Interfaces* **16**, 35841–35851 (2024).
27. Fuhrer, M. S. & Hone, J. Measurement of mobility in dual-gated MoS_2 transistors. *Nat. Nanotechnol.* **8**, 146–147 (2013).
28. Yu, Z. et al. Analyzing the carrier mobility in transition-metal dichalcogenide MoS_2 field-effect transistors. *Adv. Funct. Mater.* **27**, 1604093 (2017).
29. Buscema, M., Steele, G. A., van der Zant, H. S. J. & Castellanos-Gomez, A. The effect of the substrate on the Raman and photoluminescence emission of single-layer MoS_2. *Nano Res.* **7**, 561–571 (2014).
30. Ge, Y., Wan, W., Feng, W., Xiao, D. & Yao, Y. Effect of doping and strain modulations on electron transport in monolayer MoS_2. *Phys. Rev. B* **90**, 035414 (2014).
31. Feng, J., Qian, X., Huang, C.-W. & Li, J. Strain-engineered artificial atom as a broad-spectrum solar energy funnel. *Nat. Photon.* **6**, 866–872 (2012).
32. Lloyd, D. et al. Band gap engineering with ultralarge biaxial strains in suspended monolayer MoS_2. *Nano Lett.* **16**, 5836–5841 (2016).
33. Tyurnina, A. V. et al. Strained bubbles in van der Waals heterostructures as local emitters of photoluminescence with adjustable wavelength. *ACS Photon.* **6**, 516–524 (2019).
34. Wang, H., Zhang, C. & Rana, F. Surface recombination limited lifetimes of photoexcited carriers in few-layer transition metal dichalcogenide MoS_2. *Nano Lett.* **15**, 8204–8210 (2015).
35. Danovich, M., Zólyomi, V., Fal'ko, V. I. & Aleiner, I. L. Auger recombination of dark excitons in WS_2 and WSe_2 monolayers. *2d Mater.* **3**, 035011 (2016).
36. Verma, A., Soni, A., Sarkar, A. S. & Pal, S. K. Defect-mediated saturable absorption and carrier dynamics in tin (II) monosulfide quantum dots. *Opt. Lett.* **48**, 4641–4644 (2023).
37. Peimyoo, N. et al. Chemically driven tunable light emission of charged and neutral excitons in monolayer WS_2. *ACS Nano* **8**, 11320–11329 (2014).
38. Lien, D.-H. et al. Electrical suppression of all nonradiative recombination pathways in monolayer semiconductors. *Science* **364**, 468–471 (2019).
39. Bernardi, M., Ataca, C., Palummo, M. & Grossman, J. C. Optical and electronic properties of two-dimensional layered materials. *Nanophotonics* **6**, 479–493 (2017).
40. Dhakal, K. P. et al. Confocal absorption spectral imaging of MoS_2: Optical transitions depending on the atomic thickness of intrinsic and chemically doped MoS_2. *Nanoscale* **6**, 13028–13035 (2014).
41. Hill, H. M. et al. Observation of excitonic rydberg states in monolayer MoS_2 and WS_2 by photoluminescence excitation spectroscopy. *Nano Lett.* **15**, 2992–2997 (2015).
42. Li, H. et al. From bulk to Monolayer$_2$: Evolution of Raman scattering. *Adv. Funct. Mater.* **22**, 1385–1390 (2012).
43. Gnanasekar, P. et al. Promoter-free synthesis of monolayer MoS_2 by chemical vapour deposition. *CrystEngComm* **20**, 4249–4257 (2018).
44. Soni, A., Kushavah, D., Lu, L.-S., Chang, W.-H. & Pal, S. K. Efficient multiple exciton generation in monolayer MoS_2. *J. Phys. Chem. Lett.* **14**, 2965–2972 (2023).
45. Conley, H. J. et al. Bandgap engineering of strained monolayer and bilayer MoS_2. *Nano Lett.* **13**, 3626–3630 (2013).
46. Cun, H. et al. Wafer-scale MOCVD growth of monolayer MoS_2 on sapphire and SiO_2. *Nano Res.* **12**, 2646–2652 (2019).
47. Kang, L. et al. Epitaxial growth of highly-aligned MoS_2 on c-plane sapphire. *Surface Sci.* **720**, 122046 (2022).
48. Krustok, J. et al. Optical study of local strain related disordering in CVD-grown $MoSe_2$ monolayers. *Appl. Phys. Lett.* **109**, 253106 (2016).
49. Li, H. et al. Optoelectronic crystal of artificial atoms in strain-textured molybdenum disulphide. *Nat. Commun.* **6**, 7381 (2015).
50. Chae, W. H., Cain, J. D., Hanson, E. D., Murthy, A. A. & Dravid, V. P. Substrate-induced strain and charge doping in CVD-grown monolayer MoS_2. *Appl. Phys. Lett.* **111**, 143106 (2017).
51. Rice, C. et al. Raman-scattering measurements and first-principles calculations of strain-induced phonon shifts in monolayer MoS_2. *Phys. Rev. B* **87**, 081307 (2013).
52. Seravalli, L. et al. Built-in tensile strain dependence on the lateral size of monolayer MoS_2 synthesized by liquid precursor chemical vapor deposition. *Nanoscale* **15**, 14669–14678 (2023).
53. Liu, S. et al. Room-temperature valley polarization in atomically thin semiconductors via chalcogenide alloying. *ACS Nano* **14**, 9873–9883 (2020).
54. Zhumagulov, Y. V., Vagov, A., Gulevich, D. R., Faria Junior, P. E. & Perebeinos, V. Trion induced photoluminescence of a doped MoS_2 monolayer. *J. Chem. Phys.* **153**, 044132 (2020).

55. Basu, N. et al. Strain relaxation in monolayer MoS_2 over flexible substrate. *RSC Adv.* **13**, 16241–16247 (2023).
56. Harats, M. G., Kirchhof, J. N., Qiao, M., Greben, K. & Bolotin, K. I. Dynamics and efficient conversion of excitons to trions in non-uniformly strained monolayer WS_2. *Nat. Photon.* **14**, 324–329 (2020).
57. Castellanos-Gomez, A. et al. Local strain engineering in atomically thin MoS_2. *Nano Lett.* **13**, 5361–5366 (2013).
58. Niehues, I. et al. Strain control of exciton-phonon coupling in atomically thin semiconductors. *Nano Lett.* **18**, 1751–1757 (2018).
59. Tongay, S. et al. Defects activated photoluminescence in two-dimensional semiconductors: Interplay between bound, charged and free excitons. *Sci. Rep.* **3**, 2657 (2013).
60. Madapu, K. K., Bhuyan, C. A. & Dhara, S. Origin of bound exciton emission in CVD-grown monolayer MoS_2. *Phys. Rev. B* **108**, 085429 (2023).
61. Baniecki, J. D. et al. Strain dependent electronic structure and band offset tuning at heterointerfaces of AS_nO_3 (A=Ca, Sr, and Ba) and $SrTiO_3$. *Sci. Rep.* **7**, 41725 (2017).
62 Tian, F. et al. Strain-dependent band structures and electronic properties in Sb/Bi lateral heterostructures calculated by first principles. *Physica Status Solidi (RRL) – Rapid Res. Lett.* **15**, 2100148 (2021).
63. Dimple, Jena, N., Behere, S. D. & De Sarkar, A. The effects of different possible modes of uniaxial strain on the tunability of electronic and band structures in MoS_2 monolayer nanosheet via first-principles density functional theory. *Pramana* **89**, 2 (2017).
64. Sah, R. K., Tang, H., Shahi, C., Ruzsinszky, A. & Perdew, J. P. Effect of strain on the band gap of monolayer MoS_2. *Phys. Rev. B* **110**, 144109 (2024).
65. Wang, C., Li, S., Wang, S., Zhao, P. & Zhuo, R. First principles study of the effect of uniaxial strain on monolayer MoS_2. *Phys. E: Low-Dimens. Syst. Nanostructures* **144**, 115401 (2022).
66. Heo, S. N., Ishiguro, Y., Hayakawa, R., Chikyow, T. & Wakayama, Y. Perspective: Highly ordered MoS_2 thin films grown by multi-step chemical vapor deposition process. *APL Mater.* **4**, 030901 (2016).
67. Heo, S., Hayakawa, R. & Wakayama, Y. Carrier transport properties of MoS_2 field-effect transistors produced by multi-step chemical vapor deposition method. *J. Appl. Phys.* **121**, 024301 (2017).
68. Amin, R., Hossain, M. A. & Zakaria, Y. Interfacial kinetics and ionic diffusivity of the electrodeposited MoS_2 film. *ACS Appl. Mater. Interfaces* **10**, 13509–13518 (2018).
69. Gao, J. et al. Aging of transition metal dichalcogenide monolayers. *ACS Nano* **10**, 2628–2635 (2016).
70. Suenaga, K. et al. Surface-Mediated aligned growth of monolayer MoS_2 and in-plane heterostructures with graphene on sapphire. *ACS Nano* **12**, 10032–10044 (2018).
71. Lin, Z. et al. Controllable growth of large-size crystalline mos_2 and resist-free transfer assisted with a Cu thin film. *Sci. Rep.* **5**, 18596 (2015).
72. Yu, H. et al. Wafer-scale growth and transfer of highly-oriented monolayer MoS_2 continuous films. *ACS Nano* **11**, 12001–12007 (2017).
73. Wang, R. et al. Ultrafast and spatially resolved studies of charge carriers in atomically thin molybdenum disulfide. *Phys. Rev. B* **86**, 045406 (2012).
74. Nie, Z. et al. Ultrafast carrier thermalization and cooling dynamics in few-layer MoS_2. *ACS Nano* **8**, 10931–10940 (2014).
75. Sim, S. et al. Exciton dynamics in atomically thin MoS_2: Interexcitonic interaction and broadening kinetics. *Phys. Rev. B* **88**, 075434 (2013).
76. Shukla, A. et al. Effect of confinement on the exciton and biexciton dynamics in perovskite 2D-nanosheets and 3D-nanocrystals. *J. Phys. Chem. Lett.* **11**, 6344–6352 (2020).
77. Seo, S. B. et al. Ultrafast tunable broadband optical anisotropy in two-dimensional ReS_2. *Phys. Rev. Appl.* **18**, 014010 (2022).
78. Chen, K. et al. Experimental evidence of exciton capture by mid-gap defects in CVD grown monolayer $MoSe_2$. *NPJ 2D Mater. Appl.* **1**, 15 (2017).
79. Wu, A., Song, Q. & Liu, H. Oxygen atom adsorbed on the sulphur vacancy of monolayer MoS_2: A promising method for the passivation of the vacancy defect. *Comput. Theor. Chem.* **1187**, 112906 (2020).
80. Kc, S., Longo, R. C., Addou, R., Wallace, R. M. & Cho, K. Impact of intrinsic atomic defects on the electronic structure of MoS_2 monolayers. *Nanotechnology* **25**, 375703 (2014).
81. Lu, C.-P., Li, G., Mao, J., Wang, L.-M. & Andrei, E. Y. Bandgap, mid-gap states, and gating effects in MoS_2. *Nano Lett.* **14**, 4628–4633 (2014).
82. Liu, H.-L. et al. Temperature-dependent optical constants of monolayer MoS_2, $MoSe_2$ WS_2, and WSe_2: Spectroscopic ellipsometry and first-principles calculations. *Sci. Rep.* **10**, 15282 (2020).
83. Li, H. & Zhang, X. H. Temperature-dependent photoluminescence and time-resolved photoluminescence study of monolayer molybdenum disulfide. *Opt. Mater.* **107**, 110150 (2020).
84. Korn, T., Heydrich, S., Hirmer, M., Schmutzler, J. & Schüller, C. Low-temperature photocarrier dynamics in monolayer MoS_2. *Appl. Phys. Lett.* **99**, 102109 (2011).
85. Choi, B. K. et al. Temperature dependence of band gap in $MoSe_2$ grown by molecular beam epitaxy. *Nanoscale Res. Lett.* **12**, 492 (2017).
86. Li, H., Zhu, X., Tang, Z. K. & Zhang, X. H. Low-temperature photoluminescence emission of monolayer MoS_2 on diverse substrates grown by CVD. *J. Luminescence* **199**, 210–215 (2018).
87. Chow, P. K. et al. Defect-induced photoluminescence in monolayer semiconducting transition metal dichalcogenides. *ACS Nano* **9**, 1520–1527 (2015).
88. Wang, T. et al. Hot carrier cooling and trapping in atomically thin WS_2 probed by three-pulse femtosecond spectroscopy. *ACS Nano* **17**, 6330–6340 (2023).
89. Soni, A., Kushavah, D., Lu, L.-S., Chang, W.-H. & Pal, S. K. Ultrafast exciton trapping and exciton-exciton annihilation in large-area CVD-grown monolayer WS_2. *J. Phys. Chem. C* **125**, 23880–23888 (2021).
90. Xu, S., Yang, J., Jiang, H., Su, F. & Zeng, Z. Transient photoconductivity and free carrier dynamics in a monolayer WS_2 probed by time resolved Terahertz spectroscopy. *Nanotechnology* **30**, 265706 (2019).
91. Sun, D. et al. Observation of rapid exciton-exciton annihilation in monolayer molybdenum disulfide. *Nano Lett.* **14**, 5625–5629 (2014).
92. Cunningham, P. D., McCreary, K. M. & Jonker, B. T. Auger recombination in chemical vapor deposition-grown monolayer WS_2. *J. Phys. Chem. Lett.* **7**, 5242–5246 (2016).
93. Fan, P. et al. Trion-induced distinct transient behavior and stokes shift in WS_2 monolayers. *J. Phys. Chem. Lett.* **10**, 3763–3772 (2019).
94. Tsai, H.-S. et al. Ultrafast exciton dynamics in scalable monolayer MoS_2 synthesized by metal sulfurization. *ACS Omega* **5**, 10725–10730 (2020).
95. Chen, K. et al. Carrier trapping by oxygen impurities in molybdenum diselenide. *ACS Appl. Mater. Interfaces* **10**, 1125–1131 (2018).
96. Rao, R. et al. Dynamics of cleaning, passivating and doping monolayer MoS_2 by controlled laser irradiation. *2d Mater.* **6**, 045031 (2019).
97. Zhu, H., Yang, Y. & Lian, T. Multiexciton annihilation and dissociation in quantum confined semiconductor nanocrystals. *Acc. Chem. Res.* **46**, 1270–1279 (2013).
98. Yuan, L. & Huang, L. Exciton dynamics and annihilation in WS_2 2D semiconductors. *Nanoscale* **7**, 7402–7408 (2015).

99. Lee, H. S., Kim, M. S., Kim, H. & Lee, Y. H. Identifying multiexcitons in MoS_2 monolayers at room temperature. *Phys. Rev. B* **93**, 140409 (2016).
100. Wang, W. et al. Studying of the biexciton characteristics in monolayer MoS_2. *J. Phys. Chem. C* **124**, 1749–1754 (2020).
101. Sim, S. et al. Role of weak interlayer coupling in ultrafast exciton-exciton annihilation in two-dimensional rhenium dichalcogenides. *Phys. Rev. B* **101**, 174309 (2020).
102. Wang, H., Zhang, C. & Rana, F. Ultrafast dynamics of defect-assisted electron-hole recombination in monolayer MoS_2. *Nano Lett.* **15**, 339–345 (2015).
103. Shin, H. J., Bae, S. & Sim, S. Ultrafast auger process in few-layer $PtSe_2$. *Nanoscale* **12**, 22185–22191 (2020).
104. Hong, H. et al. Modulation of carrier lifetime in MoS_2 monolayer by uniaxial strain. *Chin. Phys. B* **29**, 077201 (2020).
105. Mondal, N., Azam, N., Gartstein, Y. N., Mahjouri-Samani, M. & Malko, A. V. Photoexcitation dynamics and long-lived excitons in strain-engineered transition metal dichalcogenides. *Adv. Mater.* **34**, 2110568 (2022).
106. Suk, S. H. et al. Sub-picosecond, strain-tunable, polarization-selective optical switching via anisotropic exciton dynamics in quasi-1D $ZrSe_3$. *Light Sci. Appl.* **13**, 240 (2024).
107. Zhang, X. et al. Unravelling the effect of sulfur vacancies on the electronic structure of the MoS_2 crystal. *Phys. Chem. Chem. Phys.* **22**, 21776–21783 (2020).
108. Wang, H., Xu, X. & Neville, A. Facile synthesis of vacancy-induced 2H-MoS_2 nanosheets and defect investigation for supercapacitor application. *RSC Adv.* **11**, 26273–26283 (2021).
109. Samy, O., Zeng, S., Birowosuto, M. D. & El Moutaouakil, A. A review on MoS_2 properties, synthesis, sensing applications and challenges. *Crystals* **11**, 355 (2021).
110. Miralrio, A., Rangel Cortes, E. & Castro, M. Electronic properties and enhanced reactivity of MoS_2 monolayers with substitutional gold atoms embedded into sulfur vacancies. *Appl. Surf. Sci.* **455**, 758–770 (2018).
111. Liu, D., Guo, Y., Fang, L. & Robertson, J. Sulfur vacancies in monolayer MoS_2 and its electrical contacts. *Appl. Phys. Lett.* **103**, 183113 (2013).
112. Yin, L. et al. Robust trap effect in transition metal dichalcogenides for advaanced multifunctional devices. *Nat. Commun.* **10**, 4133 (2019).
113. Lin, Y. et al. Enhanced emission from defect levels in multilayer MoS_2. *Adv. Opt. Mater.* **10**, 2201059 (2022).
114. Tan, A. M. Z., Freysoldt, C. & Hennig, R. G. Stability of charged sulfur vacancies in 2D and bulk MoS_2 from plane-wave density functional theory with electrostatic corrections. *Phys. Rev. Mater.* **4**, 064004 (2020).
115. Zhu, Y. et al. Room-temperature photoluminescence mediated by sulfur vacancies in 2D molybdenum disulfide. *ACS Nano* **17**, 13545–13553 (2023).
116. Ren, Z. et al. Efficient optical modulation of exciton state population in monolayer MoS_2 at room temperature. *Nanomaterials* **12**, 3133 (2022).
117. Lippert, S. et al. Influence of the substrate material on the optical properties of tungsten diselenide monolayers. *2d Mater.* **4**, 025045 (2017).
118. Korapati, P., Kumari, A. K., Kosuri, Y. R., Priya, B. K. & Dodda, V. R. K. R. The effect of substrate on enhancing the sensing properties of nitric oxide gas detection of MoS_2 thin film. *Emergent Mater.* **7**, 1779–1791 (2024).
119. Kushavah, D., Mushtaq, A. & Pal, S. K. Ultrafast and nonlinear optical properties of two-dimensional MO-doped dual phase inorganic lead halide perovskite. *J. Phys. Chem. C* **127**, 20014–20025 (2023).

Acknowledgements

AS and SKP gratefully acknowledge the financial support from the Scienceand Engineering Research Board (SERB), Government of India (Grant No.CRG/2018/003045). All authors thank the Advanced Materials ResearchCentre (AMRC) of IIT Mandi for providing experimental facilities. We alsoacknowledge the assistance of ChatGPT for editing English.

Author contributions

A.S. has done absorption, Raman, photoluminescence and XPS measurements. A.S. and N.K. did transient absorption measurements. A.S. analyzed the experimental data, prepared figures and draft the manuscript text. Y.Y.S. prepared samples under the supervision of W.H.C. H.S. and A.D.S. carried out ab initio calculations and wrote the theoretical part of the manuscript. S.K.P supervised experimental works and corrected the manuscript text. All authors reviewed the manuscript.

Declarations

Competing interests

The authors declare no competing interests.

Additional information

Supplementary Information The online version contains supplementary material available at https://doi.org/10.1038/s41598-025-92188-1.

Correspondence and requests for materials should be addressed to S.K.P.